Check for
updates

Droplet Evaporation-Based Approach for Microliter Fuel Property Measurements

Wanjun Dang[1] · Mohana Gurunadhan[1] · William Ard[1] · Ingmar Schoegl[1] · Shyam Menon[1]

Abstract

Small-volume, high-throughput screening techniques are sought to enable downselection from a large candidate pool of bio-blendstocks to a select few, having physical properties consistent with requirements of downsized, turbo-boosted internal combustion engines. This work presents a droplet evaporation-based approach to predict heat of vaporization, vapor pressure, diffusion coefficient, and Lennard–Jones parameters for an unknown fuel. Two different schemes, considering the isothermal evaporation of a moving droplet in ambient air, are proposed, which combine droplet velocity and temperature measurements, with some known properties to predict unknown properties. The schemes utilize an inverse solution of a transient model of droplet evaporation solved in an iterative fashion. A baseline scheme, which only requires droplet size change measurements, is evaluated using test data for three liquid fuels, comprising of alkanes and alcohols, as obtained in a temperature-controlled chamber. Results yield temperature-dependent heat of vaporization and vapor pressure predictions within 10 % and 22 %, respectively, of reference values. The advanced scheme, which additionally requires droplet temperature measurement, is numerically evaluated in the current work and will be experimentally validated in future efforts. The advanced scheme is found to significantly improve prediction quality, with deviations less than 2 % and 1 % for heat of vaporization and vapor pressure, while also predicting diffusion coefficient and Lennard–Jones parameters within 5 % and 8 %, respectively. The combined set of approaches, which primarily track droplet evaporation, can be incorporated into a small-volume, high-throughput fuel screening process.

Keywords Abramzon–Sirignano model · Diffusion coefficient · Droplet evaporation · Heat of vaporization · Lennard–Jones parameters · Vapor pressure

---

Wanjun Dang, Mohana Gurunadhan, William Ard, Ingmar Schoegl and Shyam Menon have contributed equally to this work.

Extended author information available on the last page of the article

Abbreviations

Symbols
P	Pressure
Y	Mass fraction
$\dot{m}_l$	Evaporation rate
ρ	Density
k	Thermal conductivity
χ	Mass diffusion coefficient
Re	Reynolds number
Sc	Schmidt number
Sh	Sherwood number
H_F	Heat of vaporization
R_u	Universal gas constant
B_T	Heat transfer number
σ	LJ length
m_l	Droplet mass
T	Temperature
D	Diameter
u	Droplet velocity
C_p	Specific heat
μ	Dynamic viscosity
MW	Molecular weight
Nu	Nusselt number
Pr	Prandlt number
Nu	Nusselt number
C_D	Drag coefficient
B_M	Mass transfer number
g_0	Gravitational acceleration
$\dfrac{\epsilon}{k_b}$	LJ energy parameter

Subscripts and Qualifying Notations
$\bar{\phi}$	Property ϕ at film temperature and mass fraction Eq. A4
F	Fuel
c	Carrier gas
i	Interface
$boil$	Boiling point
f	Film
vap	Vapor
l	Liquid
∞	Far field ambient

1 Introduction

Fuel spray plays a key role in the overall performance and emissions of direct-injected, liquid hydrocarbon-fueled internal combustion (IC) engines. Fuel physical properties have a direct impact on the efficacy of in-cylinder processes such as spray breakup, atomization, evaporation, and fuel-air mixing. Spray breakup through atomization, and its penetration into the cylinder volume are impacted by fuel surface tension and viscosity [1]. Subsequent evaporation and fuel-air mixing are directly coupled to the heat of vaporization (*HOV*) and vapor pressure (P_{vap}) of the fuel, as dictated by the ambient conditions surrounding the fuel droplets [2]. *HOV* is the energy required for phase change of the liquid fuel. P_{vap} is a measure of the pressure exerted by the fuel vapor in thermodynamic equilibrium condition with its liquid phase. *HOV* and P_{vap} can be related to each other through the Clausius–Clapeyron equation [3],

$$ln(P_{vap}) = -HOV/(RT) + C, \tag{1}$$

where P_{vap} is the vapor pressure at the corresponding temperature *T*, *R* is the gas constant, and *C* is the intercept of the linear fit from plotting the natural log of P_{vap} against temperature.

HOV affects in-cylinder thermodynamics through the fuel droplet evaporation process, which results in cooling of the in-cylinder charge. The subsequent reduction in charge temperature and corresponding increase in intake air density results in improved volumetric efficiency of gasoline engines, particularly at part load conditions [4]. Evaporative cooling also facilitates knock suppression, with previous studies on downsized, turbo-boosted engines demonstrating an increase of fuel octane rating by 5 units [5], and an increase in the allowable compression ratio by about 1 unit [6]. Several studies have pursued this strategy and demonstrated the impact of ethanol and other alcohol blends on engine knock [6–9]. Vapor pressure is widely used in assessing the quality of gasoline, as relating to the volatility of the fuel, which has a direct influence on engine performance as well as fuel production and transportation logistics. Fuels with lower vapor pressure are harder to vaporize resulting in poor combustion efficiency [10]. On the other hand, fuels with high vapor pressure can generate volatile organic compounds leading to uncontrolled air–fuel ratio affecting the combustion process.

Standard testing approaches and procedures have been established for measuring *HOV* and vapor pressure. A differential scanning calorimeter (DSC)/thermogravimetric analysis (TGA) is a standard tool used in *HOV* measurement of fuels and blends. A Q600-series model from TA instruments used in previous studies [11] utilizes sample sizes ranging from 0.04 cc to 0.1 cc (40–100 μl) and calculates *HOV* on the basis of heat energy required for sample evaporation. Gasoline volatility is typically expressed through the Reid Vapor Pressure (RVP). RVP represents the fuel industry standard for vapor pressure and is the value measured at 37.8 °C in a container with a vapor to liquid ratio (V/L) of 4:1 [12]. RVP can be measured through a variety of Reid methods including ASTM D-323 and D-4953, which are referred to as the original and dry Reid methods, as well as D-5191 and D-5482 which are

referred to as miniaturized methods [13–15]. Sample sizes range from 100 cc for the original and dry Reid methods to between 1 cc and 10 cc for the miniaturized methods. ASTM D-6378 is yet another measurement procedure requiring 5–15 cc particularly addressing limitations of previous methods for dealing with volatile fuel components. All of the above-mentioned RVP measurement methods except D-323 are capable of operation with oxygenated fuels which is relevant to this work.

While standard techniques of *HOV* and vapor pressure measurement as described above operate with fuel samples of $\mathcal{O}(\text{ml})$, this study is motivated by a desire to operate with fuel samples of $\mathcal{O}(\mu l)$ and high throughput. This will enable rapid-screening approaches as desired by the DOE's (Department of Energy) Co-Optima initiative to identify potential gasoline blendstocks with viable biomass-derived production pathways [16]. This work builds on previous efforts by the authors to develop small-volume, high-throughput measurement approaches for surface tension and viscosity [17, 18] and extends it to measurement of additional properties including *HOV*, vapor pressure, diffusion coefficient, and Lennard–Jones (LJ) parameters. Besides the standard techniques discussed earlier, a number of molecular structure-based approaches for vapor pressure and *HOV* estimation have been also developed [19–23]. However, the droplet evaporation-based approach pursued in this work has the advantage that it conveniently fits within a process workflow, whereby droplet oscillation and droplet combustion are additionally used to measure physical and combustion-kinetic relevant properties [24].

The paper is laid out as follows. The numerical approach involving a zero-dimensional transient droplet evaporation process for stationary and moving liquid fuel droplets is discussed. Two different schemes utilizing experimental data and the 0D simulation are presented. The experimental setup and procedure used to measure fuel droplet evaporation rate at controlled temperature conditions is discussed. Results obtained from a baseline scheme requiring only droplet size change measurements are presented for *HOV* and vapor pressure predictions. Tested fuels include a pure alkane, a gasoline surrogate (alkane blend), and a bio-blendstock (alcohol). Next, results are presented for *HOV*, vapor pressure, diffusion coefficient, and LJ parameters as can be obtained from a more advanced scheme requiring additional inputs including droplet velocity and temperature. Results are discussed and finally conclusions are presented.

2 Approach

As described in the introduction, this work is motivated by development of techniques for *HOV* and vapor pressure measurement of liquid hydrocarbon fuels, suitable for use in high-throughput, rapid-screening approaches for bio-derived gasoline blendstocks. In previous related efforts [17, 18], a droplet oscillation-based approach to measure surface tension and viscosity of fuels at ambient and elevated temperatures has been presented. In these studies, droplets were generated using a piezo-electric droplet generator capable of operating with μl samples. In an effort to constrain the sample volume requirement, the approach proposed in this work utilizes the same droplet generation hardware. Droplet oscillation, which begins at the point
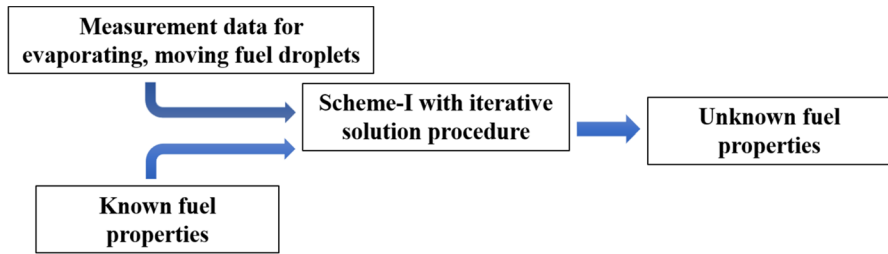
Fig. 1 Fuel property prediction approach using droplet evaporation measurements

of droplet generation and ends a short while after, can be used to measure surface tension and viscosity. The proposed approach intends to use evaporation processes of the droplet post oscillation, to measure *HOV* and vapor pressure. This provides a streamlined approach utilizing the minimum quantity of the fuel sample. Besides being capable of making measurements with small sample sizes, the timescale of the entire process from the point of droplet jetting to complete evaporation is small ($\mathcal{O}$(ms)), thus ensuring compatibility for a rapid-screening approach. Finally, with minor modifications and packaging, it is possible to integrate the physical property evaluation techniques based on droplet oscillation and evaporation with chemical kinetic property evaluation techniques being developed using a micro-combustor setup [24].

A liquid fuel droplet subjected to a controlled temperature environment undergoes evaporation under stationary or moving conditions. The evaporation process for small droplets involving heat and mass transfer is controlled primarily by the ambient conditions and liquid properties including *HOV* and to a smaller degree by second-order effects such as circulation within the droplet and water condensation on the droplet surface. A large body of work has been carried out to model droplet evaporation processes incorporating various levels of complexity, which are detailed in a number of review publications [25–27]. The approach used in this work is to use an appropriate droplet evaporation model to calculate fuel properties of interest including *HOV* and vapor pressure, using measurements obtained from experiments with moving, evaporating droplets. Measurements can include various parameters including droplet size, velocity, and temperature as will be discussed in further detail later in this section. The approach is illustrated schematically in Fig. 1.

A similar approach was followed by Ray [28] who used observations of size change of evaporating droplets at stationary conditions as obtained through droplet levitation, to estimate ultra-low vapor pressures of fluids used in aerosol research. Ray used a Maximum Likelihood Estimation (MLE) approach to determine fluid physical properties including *HOV* and vapor pressure as well as molecular dynamic parameters such as the parameters relating to the Lennard–Jones potential. This approach differs from Ray's work in that the focus is on using moving droplets to allow a simpler experimental setup without the need to levitate droplets in a constant temperature chamber. This work utilizes the Abramzon and Sirignano (AS) model [25] to simulate the evaporation process of moving droplets. The Abramzon
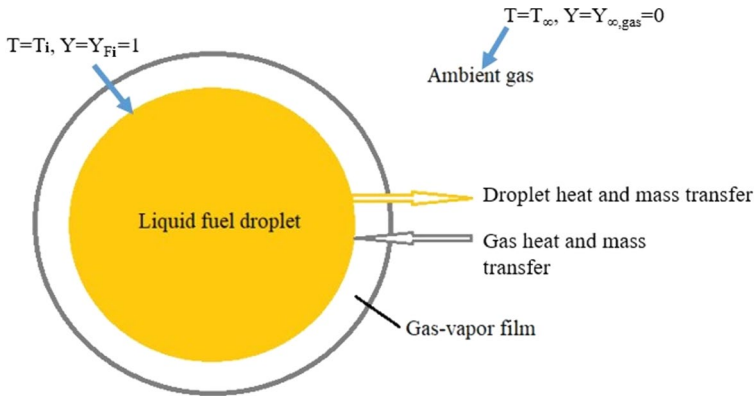
Fig. 2 Droplet evaporation model incorporating the liquid-vapor film

model incorporates Stefan flow and effects of convective heat and mass transfer using a "film theory", which in essence introduces a vapor–gas film between the droplet surface and ambient atmosphere, effectively providing resistance to heat and mass exchange as shown schematically in Fig. 2. Model assumptions include quasi-steady heat and mass transfer, temperature-dependent thermo-physical properties, uniform temperature and fuel vapor concentration on the droplet surface, spatially uniform but time-varying droplet temperature, and no velocity field within the droplet.

Source terms considered in the model include those for:

- Droplet velocity:

$$\frac{du}{dt} = -\frac{3C_D\bar{\rho}_f}{4D\rho_l}(u - u_\infty)^2 + g_0\left(1 - \frac{\bar{\rho}_f}{\rho_l}\right), \tag{2}$$

where $\bar{\rho}_f$ is the density of the vapor in the film, g_0 is the acceleration due to gravity, C_D is the drag coefficient, u is the droplet velocity, u_∞ is the ambient gas velocity, D is the droplet diameter and ρ_l is the liquid density.

- Droplet diameter:

$$\frac{dD}{dt} = -\frac{2\dot{m}_l}{\pi\rho_l D^2}, \tag{3}$$

where $\dot{m}_l$ is the net instantaneous evaporation rate of the droplet in $kg \cdot s^{-1}$.

- Droplet temperature:

$$\frac{dT_l}{dt} = \frac{\dot{Q}_l}{m_l C_{pl}}, \tag{4}$$

where $\dot{Q}_l$ is the rate of heat transfer to the liquid droplet and m_l is the mass of the droplet.

In the above transient governing equations, C_D, $\dot{m}_l$ and $\dot{Q}_l$ are defined based on the operating conditions and properties of the fuel and carrier gas. From the mass and energy balance equations at the interface, evaporation rate, $\dot{m}_l$ is defined as:

$$\dot{m}_l = \pi \bar{\rho}_f \bar{\chi}_{fc} D \mathrm{Sh}^* \ln(1 + B_M) = \pi \frac{\bar{k}_f}{\bar{C}_{pF}} D \mathrm{Nu}^* \ln(1 + B_T), \qquad (5)$$

where,

$$B_M = \frac{(Y_{Fi} - Y_{F\infty})}{(1 - Y_{Fi})}, \quad B_T = \frac{\bar{C}_{pF}(T_\infty - T_i)}{H_F(T_i) + \frac{\dot{Q}_l}{\dot{m}_l}}. \qquad (6)$$

In the above equations, $\bar{\chi}_{fc}$ is the diffusivity in the film, B_M refers to the mass transfer number, calculated from fuel vapor mass fraction at the droplet interface (Y_{Fi})and in the far field ambient ($Y_{F\infty} = 0$) and B_T refers to the heat transfer number, defined using the droplet interface temperature T_i, far field ambient temperature T_∞, heat of vaporization of the fuel H_F evaluated at droplet temperature T_i and the average specific heat of fuel vapor in film ($\bar{C}_{pF}$) evaluated at film temperature $\bar{T}_f$. Nu^* and Sh^* are the modified Nusselt number and Sherwood number, respectively, for a spherical droplet, considering the effect of blowing. The definition of Nusselt number, Sherwood number and film temperature, based on the work of Abramzon *et al*. [25], is provided in Appendix A. Nu^* is a function of Reynolds number (Re) and Prandtl number (Pr), while Sh^* is a function of Re and Schmidt number (Sc). For the droplet diameter and velocity scales considered in the present work, Re is found to be <0.1 and the effect of velocity through Re on property predictions can be neglected. However, this effect should be considered for larger droplets with higher velocities. The subscript f refers to the gas phase properties in the gas-vapor film, l refers to the liquid properties, i indicates the properties at the liquid surface (liquid-gas interface) and the fuel vapor properties are indicated by subscript F. The interface temperature, $T_i = T_l$, considering infinite thermal conductivity for the droplet, which disregards spatial temperature gradients in the droplet.

The net heat transfer rate $\dot{Q}_l$ can be evaluated using the combined equations of heat transfer number (Eq. 6) and interfacial energy balance (Eq. 5). In the transient equation for droplet velocity (Eq. 2), drag coefficient C_D is based on the correlation for 'standard drag curve' provided in the work of Putnam et. al [29] , defined as:

$$C_D = \frac{24}{\mathrm{Re}} \left\{ 1 + \frac{\mathrm{Re}^{2/3}}{6} \right\}, \qquad (7)$$

where *Re* is the Reynolds number, defined as $\frac{\bar{\rho}_f D |u - u_\infty|}{\bar{\mu}_f}$. All the gas properties in the film are defined as a function of average fuel vapor mass fraction $\bar{Y}_f$, in the film and average temperature of the film ($\bar{T}_f$). The equations used for film properties, used in the current work, are detailed in Appendix A.

In the conventional AS method, the governing equations given by Eqs. 2, 3, 4, and 5 are solved using an explicit transient solver, with fuel transport properties and
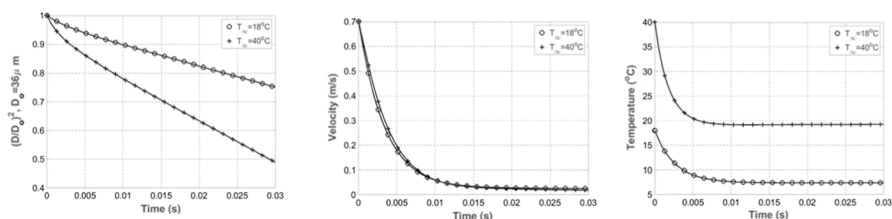
Fig. 3 Predictions for droplet evaporation using the AS model for PRF 84 at two different ambient temperatures showing variation of the square of the droplet diameter, droplet velocity, and droplet temperature as a function of time

Table 1 Summary of required inputs and predicted outputs using Scheme-I and Scheme-II

	Input data		Numerical predictions
	Measurements	Properties	
Scheme-I	$D, \dfrac{dD^2}{dt}$	Density (liquid, vapor)	Vapor pressure, P_{vap}
		Viscosity	Heat of vaporization, H_F
		Thermal conductivity	
		Specific heat	
		Diffusion coefficient	
		Boiling point	
Scheme-II	$D, \dfrac{dD^2}{dt}$	Density (Liquid, vapor)	Vapor pressure, P_{vap}
	$u, \dfrac{du}{dt}$	Viscosity	Heat of vaporization, H_F
	T_i	Thermal conductivity	Diffusion coefficients
			Lennard–Jones, (σ, ϵ)
			Boiling point, (T_{boil})

initial conditions as the input. It is noticed, based on the simulation of fuel droplets of research interest, that after the initial transients, droplet temperature (T_i) and velocity reach a quasi-steady-state and the square of droplet diameter (D^2) exhibits a quasi-linear behavior (constant slope) with time. This is illustrated by simulation results shown in Fig. 3 where the evaporation process of a droplet of PRF 84 was modeled using the AS model for two different ambient air temperatures. In the present work, it is desired to implement an inverse AS algorithm, wherein, measurement data from observations of droplet evaporation at controlled conditions will be used as inputs to estimate unknown fuel physical properties. In pursuing this approach, it is realized that the logic described above can be implemented in different ways depending on which quantities are measured in the experiments. Further, in addition to the measured quantities, some physical properties for the unknown fuel are required as inputs to the algorithm. These details are summarized in Table 1. The table provides details of the required measurement and physical property inputs
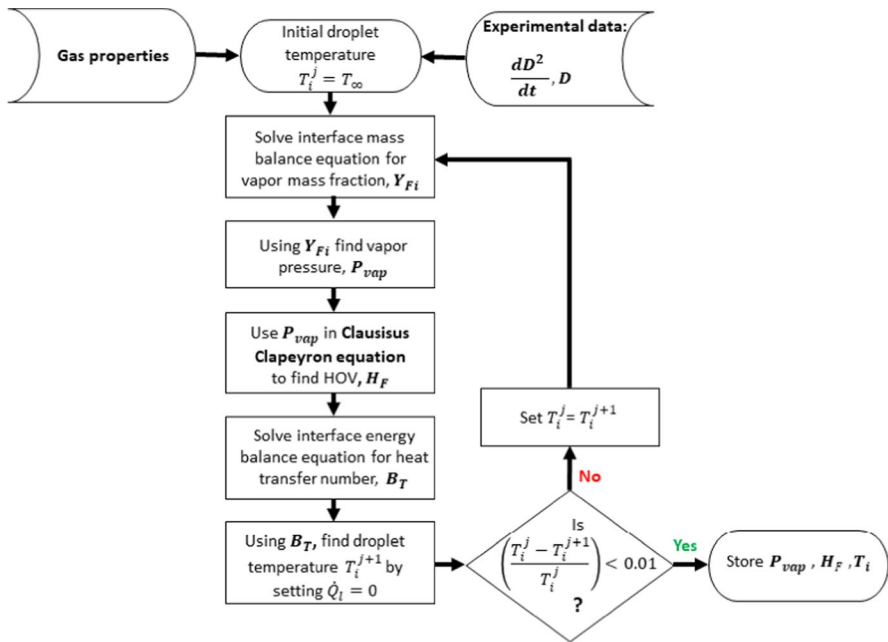
Fig. 4 Approach used in *HOV* and vapor pressure estimation using measurements and the droplet evaporation model as implemented through Scheme-I

along with the numerical predictions that can be made utilizing the inverse AS algorithm. Note that properties mentioned in the table pertain to the values for the fuel vapor. Further, numerical predictions obtained for fuel physical properties correspond to those at a steady-state temperature (T_i), as reached by the droplet during the evaporation measurements in the experiment.

Table 1 summarizes two different schemes which utilize measurements along with input data for known physical properties to give numerical predictions for unknown physical properties. As the number of measured quantities increases from Scheme-I to Scheme-II, the required number of known physical properties to be used as inputs to the algorithm decreases. Numerical predictions listed for each Scheme represents temperature-dependent values that can be obtained from the calculations except for Lennard–Jones parameters which are temperature-independent. In the present work, the major focus is on predictions of temperature-dependent *HOV* and vapor pressure. Accordingly, the viability of Scheme-1 as summarized in Table 1 is now demonstrated using experimental measurements and the inverse droplet evaporation model approach.

Details of Scheme-I are summarized in Table 1 and shown as a flowchart in Fig. 4. Droplet diameter and the quasi-linear slope of change in square of droplet diameter (D^2) with time, are provided by the experiment. Fuel vapor properties are evaluated using empirical/analytical equations described in Appendix A. Using these inputs, droplet temperature (T_i), temperature-specific vapor pressure (P_{vap}) and

heat of vaporization (H_F) can be evaluated using an iterative approach. The pertinent steps of the Scheme-I algorithm are as listed below:

1. To start the algorithm, the initial droplet temperature is assumed to be equal to far field ambient temperature ($T_i = T_\infty$). This temperature will be corrected in an iterative manner.
2. Using the droplet temperature (T_i), and experimental data and property inputs as listed in Table 1, the interfacial mass balance equation is solved for fuel vapor mass fraction at the droplet interface. Accordingly, Eq. 5 can be rewritten as an implicit function of droplet temperature and interface fuel mass fraction.

$$\dot{m}_l - \pi \bar{\rho}_f \bar{\chi}_{fc} D\mathrm{Sh}^* ln(1 + B_M) = F(Y_{Fi}, T_i) = 0. \tag{8}$$

   The above equation can be solved for unknown interface mass fraction Y_{Fi}, using any standard root finding technique. It is to be noted that the evaporation rate ($\dot{m}_l$) and droplet diameter (D) used in Eq. 8 correspond to values after a steady-state droplet temperature is achieved.
3. The interface mass fraction (Y_{Fi}) is utilized to find the instantaneous vapor pressure of the droplet, which is defined as

$$P_{vap} = P_\infty \left\{ \frac{Y_{Fi}MW_c}{MW_F + Y_{Fi}(MW_c - MW_F)} \right\}, \tag{9}$$

   where MW is the molecular weight of carrier gas (subscript 'c') and fuel (subscript 'F'), calculated using a mole weighted average.
4. With vapor pressure P_{vap} as the input, Heat of vaporization is evaluated using the Clausius–Clapeyron equation, as shown below:

$$H_F = -\ln\left(\frac{P_{vap}}{P_\infty}\right)\frac{R_u}{MW_F\left[\frac{1}{T_i} - \frac{1}{T_{boil}}\right]}, \tag{10}$$

   where T_{boil} is the fuel boiling point at the ambient pressure during the experiment.
5. The interface mass fraction is further utilized to evaluate the heat transfer number B_T. Similar to step 2, the interfacial energy balance equation, Eq. 5, can be rewritten as an implicit function of B_T, T_i and Y_{Fi}, given by:

$$\dot{m}_l - \pi \frac{\bar{k}_f}{\bar{C}_{pF}} D\mathrm{Nu}^* ln(1 + B_T) = G(Y_{Fi}, T_i, B_T) = 0. \tag{11}$$

   The above equation is solved for unknown heat transfer number B_T, using any standard root finding technique.
6. As observed from simulations using the AS model, the fuel droplet reaches a quasi-steady temperature, after the initial transients, which implies that the net heat transfer rate, $\dot{Q}_l = 0$. Using this observation, the equation for heat transfer number B_T (Eq. 6), is modified for the unknown droplet temperature T_i.
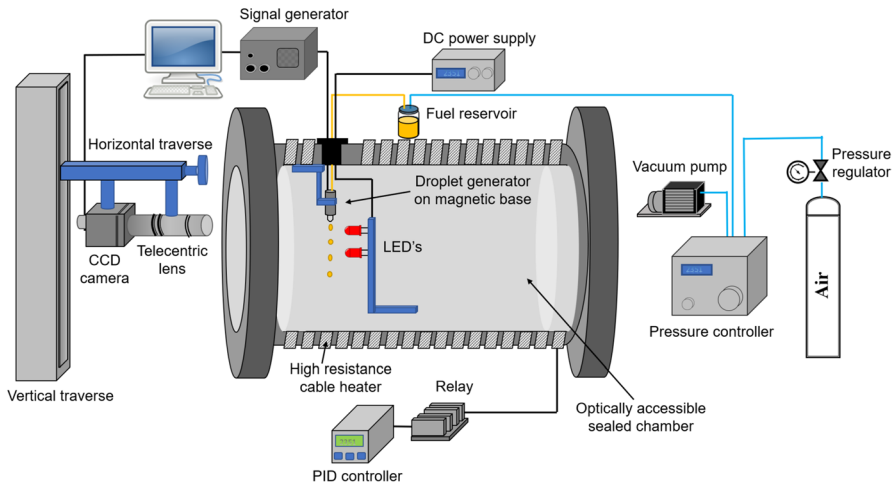
Fig. 5 Droplet evaporation experimental setup

$$T_i = \frac{-B_T H_F}{\bar{C}_{pF}} + T_\infty. \tag{12}$$

7. The droplet temperature is updated using the above value and the Steps 1 to 6 are repeated until the change in temperature, from the previous iteration, is negligible (until convergence). In the numerical trials conducted, convergence was observed in less than 15 iterations.

The algorithm Scheme-I is now used with evaporation measurements for various fuels of interest to demonstrate the validity of the approach. A detailed listing of steps to accomplish Scheme-II as summarized in Table 1 is provided in Appendix A.

3 Experiment

3.1 Experimental Setup

The experimental setup for droplet evaporation is shown schematically in Fig. 5. A piezoelectric droplet generator (Microfab PH-41, 30 μm nozzle) is placed inside a closed, cylindrical metal chamber, and used to inject a continuous stream of droplets into the chamber. A PID controller (Extech 48VFL) along with a heating element wrapped around the chamber are used to control the chamber temperature. Fuel is supplied to the droplet generator from a reservoir kept outside the chamber at room temperature(22 °C). A signal generator (Microfab JetDrive V (CT-M5-01)) provides pulses to actuate the droplet generator. The piezoelectric element on the actuator expands or contracts according to the polarity of the signal. Droplets are formed at the nozzle tip as a result of the fast deformation of the piezoelectric material. A pressure controller (MicroFab CT-PT-21) is used to select positive or negative back

pressure to sustain a balancing force on the fluid column at the exit plane of the nozzle. The back pressure is provided by a compressed air source and a vacuum pump (Koge electronics, KPV14A-6A), which, respectively, provide positive and negative back pressures to the pressure controller.

The frequency of the waveform pulse controls the droplet spacing. A machine vision camera (Sentech STC-MB33USB) mounted on a vertical traverse is used to obtain a live video of the droplet trail within the chamber. Images are extracted from the video for processing. The camera has optical access into the chamber through the quartz windows located on either side of the pressure chamber. The camera has a resolution of 4.56 μm/pixel using a Precise Eye lens and adapter. The light source for the camera is comprised of four LED's (Broadcom HLMP- CM1A-560DD), which are soldered on a circuit board located inside the chamber and provided with constant voltage using an external power supply (BK Precision Model 1621A).

3.2 Measurement Procedure

To conduct the tests, the chamber doors are closed and air is cycled through the chamber to remove any remnant fuel vapor from previous tests. All tests were conducted at atmospheric pressure. Next, the temperature controller is set to the desired set-point for chamber temperature. Chamber temperature is monitored at different locations until they reach steady-state values. This typically takes about 30–40 min. Once the desired temperature is reached inside the chamber, the back pressure controller is used to purge some of the fuel thereby producing a well-defined liquid meniscus which can be seen from the camera interface to a computer. Next, using the back pressure controller, the meniscus is carefully aligned with the exit plane of the glass nozzle. Once aligned, the desired waveform pulse is applied to produce the liquid droplet train with the required frequency. The camera is used to take a live video of the droplet trail at various downstream locations from the nozzle by moving it using the vertical traverse. Distance measurements are facilitated by an image calibration that provide a pixel to micron conversion. Using the calibration, droplet size and location from the nozzle exit are determined.

3.3 Image Processing

Image processing and analysis to capture the droplet edge and estimate droplet diameter was carried out using a custom Matlab package. The process includes background subtraction, batch cropping, anisotropic filtering, and edge detection by a subpixel method to capture the droplet shape. A detailed description of these steps can be found in previous work [17].

3.4 Fuels Tested

Fuels of interest to this work comprise of pure components and blends which have been researched as part of the DOE Co-Optima program to develop bio-blendstocks for use in advanced internal combustion (IC) engines. While this includes a large

Table 2 Properties of fuels tested in this work as relevant for use in advanced SI engines [38, 39]

Name	Functional group	Formula	Boiling point	Vapor pressure @ 100 °F	HOV @ 25 °C
n-heptane	Alkane	C_7H_{16}	98.4	11.1	364.8
Isobutanol	Alcohol	$C_4H_{10}O$	108	3.3	692.5
PRF 84	Blend	16 % C_7H_{16}, 84 %C_8H_{18}	98.7	11.6	319.8
			°C	kPa	kJ·kg^{-1}

number of pure components and blends, the current work focuses on a subset of these as listed in Table 2. PRF 84 represents a two-component blend containing 84 % *iso*-octane (Acros Organics, 99.5 %) and 16 % *n*-heptane (Acros Organics, 99.5 %) by volume. *n*-heptane has a Cetane number similar to that of commercial diesel fuel and has been used as a diesel surrogate in studies of advanced combustion strategies including Homogeneous Charge Compression Ignition (HCCI) [30] and Reactivity Controlled Compression Ignition (RCCI) [31]. PRF 84 on the other hand represents a simple two-component gasoline surrogate used in studies on conventional Spark Ignition IC engines [32]. Isobutanol has been identified by DOE's Co-Optima program as being one of the top ten bio-blendstocks for turbocharged gasoline engines [33] and is seen as a potential second generation biofuel that can be viably sourced from biomass [34].

Table 2 lists reference values for various fuel physical properties including vapor pressure measured at 100 °F (37.8 °C), which can be referred to as True Vapor Pressure (TVP). RVP differs from TVP in that RVP measurement requires evaluating vapor pressure at 100 °F and a vapor/liquid ratio of 4:1. The proposed approach discussed in this work provides an estimation of TVP, where RVP is typically less than TVP [35]. Correlations between TVP and RVP have been presented in previous work [36, 37]. In this work, temperature-dependent TVP is the output generated by the property measurement approaches, which is used to evaluate TVP at a reference temperature of 100 °F (37.8 °C) for comparison with literature data.

4 Results and Discussion

4.1 Measurements

Figure 6 shows the evaporation rate expressed as dD^2/dt as a function of ambient temperature for the three different fuels tested in this study. As can be observed, dD^2/dt increases with temperature for all fuels as expected. Further, dD^2/dt for *n*-heptane closely tracks that of PRF 84 given that the second component making up PRF 84 (*iso*-octane) has a volatility very similar to that of *n*-heptane. On the other hand isobutanol has a lower vapor pressure (Table 2) resulting in a lower evaporation rate for the same ambient temperature. Figure 6 also shows uncertainty estimates in the form of individual error bars for each data point. The
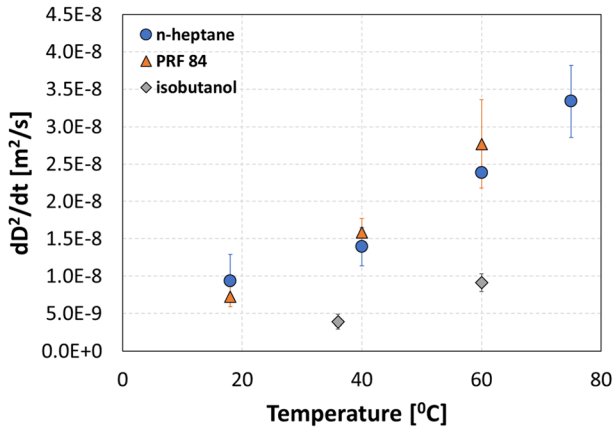
Fig. 6 Evaporation rate as expressed by the rate of change for diameter-squared as a function of ambient air temperature for the fuels tested in this work

uncertainty values represent fluctuations when evaporation rate measurements are repeated for a given fuel at a certain ambient temperature condition. They are estimated using a Student's t-distribution as appropriate for a small sample size for a confidence interval of 95 %. They result from uncertainty induced by the resolution of the imaging setup and subsequent edge detection techniques. The measured evaporation rate can be compared with a predicted value based on calculations using the AS model at identical conditions. Figure 7 shows the difference between measured and predicted values as a function of temperature. As observed in Fig. 7, the % deviation decreases for all cases with increase in temperature. This is attributed primarily to increasing change in droplet size over
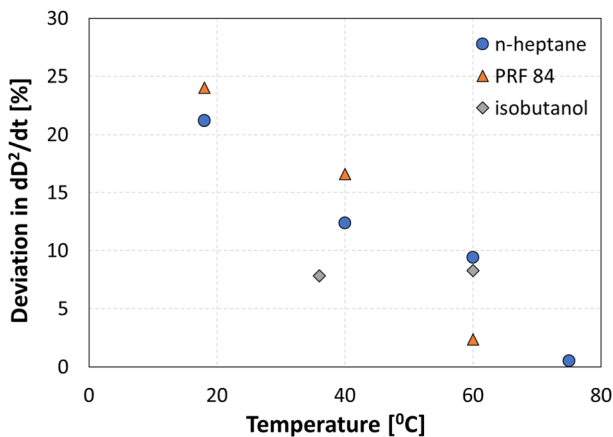

Fig. 7 Deviation in measured evaporation rate from value predicted by the droplet evaporation model as a function of ambient air temperature

Table 3 Results from calculations using Scheme-I

Fuel	Temperature	HOV [38]			Vapor pressure [3]		
		Predicted	Reference	Deviation	Predicted	Reference	Deviation
n-heptane	18	340 ± 49	374	9.1	2.78 ± 1.0	2.41	15.4
	40	390 ± 36	367	6.3	3.86 ± 0.7	4.6	16.1
	60	370 ± 5	363	1.9	6.51 ± 0.1	6.84	4.8
	75	364 ± 39	360	1.1	8.44 ± 1.2	8.71	3.1
PRF 84	18	343 ± 21	328	4.6	2.04 ± 0.4	2.60	21.5
	40	339 ± 20	323	5.0	4.13 ± 0.5	4.88	15.4
	60	325 ± 45	318	2.2	6.83 ± 1.4	7.34	6.9
Isobutanol	36	676 ± 60	690	2.0	1.39 ± 0.3	1.44	3.5
	60	673 ± 46	674	0.1	3.02 ± 0.4	3.18	5.0
	°C	kJ·kg^{-1}		%	kPa		%
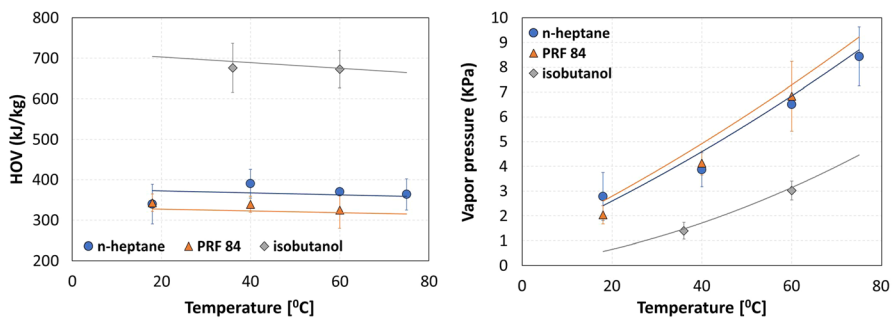
Fig. 8 HOV and vapor pressure predictions as a function of ambient air temperature for the three fuels tested in this work

the course of the observation period due to higher evaporation rates resulting in lower sensitivity to error sources.

4.2 Physical Property Predictions Using Scheme-I

Table 3 shows the results obtained from Scheme-I calculations using experimental measurements reported in Fig. 6. Predicted values for temperature-dependent HOV and vapor pressure for the three fuels tested in this work are presented along with reference values obtained from literature. It should be noted that data presented in Table 3 and further plotted in Fig. 8 are results averaged over multiple experimental data sets. Table 3 includes uncertainties calculated using Student's t-distribution as discussed earlier. Deviation reported in Table 3 is computed as the % difference between predicted and reference values.
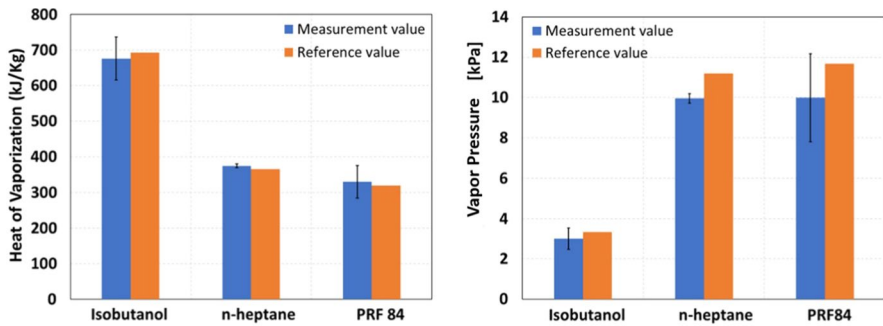
Fig. 9 Measurement results compared with reference data for *HOV* at 25 °C and TVP estimated at 37.8 °C. Both temperatures refer to the fuel temperature

Figure 8 shows predicted *HOV* and vapor pressure plotted as a function of ambient temperature. Results presented in Table 3 and Fig. 8 indicate a deviation of 0.1 % to 9 % in *HOV* prediction and 3 % to 22 % in vapor pressure prediction. Reference data are overlaid on the plots for direct comparison with the predicted data. As observed in figure, *HOV* is relatively insensitive to temperature. Vapor pressure on the other hand, shows higher sensitivity and increases with temperature. Figure 8 also shows a higher *HOV* for isobutanol, which is also consistent with its lower vapor pressure, given its lower volatility. Predicted results for *n*-heptane and PRF 84 closely follow each other consistent with the similar evaporation rate for both fuels as presented in Fig. 6.

Figure 9 shows bar charts comparing predictions for *HOV* at 25 °C and TVP at 37.8 °C of the three fuels tested in this work. *HOV* is obtained by interpolating data shown in Fig. 8. TVP corresponding to a fuel temperature of 37.8 °C is evaluated using the Clausius–Clapeyron equation (Eq. 10). The deviation in *HOV* for predictions as compared to reference values is observed to be in the range of 2 % to 3 %. However, for TVP, higher deviations are observed in the range of 10 % to 15 %. While the source for the deviations is likely the error in droplet evaporation rate measurement, the results also signify the sensitivity of vapor pressure to *HOV* through the use of the Clausius–Clapeyron equation. As seen from Eq. 10, small errors in *HOV* and droplet temperature can lead to large error in vapor pressure due to the exponential nature of the relationship. This is also illustrated by the results in Fig. 10 where the % error induced in vapor pressure calculations is correlated to % error incurred in *HOV* calculations.

4.3 Physical Property Predictions Using Scheme-II

Section 4.2 discussed the use of Scheme-I as summarized in Table 1 to estimate *HOV* and vapor pressure given measurements of droplet size change as a function of time during the evaporation process. Currently there are no diagnostics for droplet temperature measurement. This precludes the use of Scheme-II with complementary experiments to improve upon the number and quality of predicted fuel properties as summarized in Table 1. In the absence of experimental data to facilitate

Fig. 10 Error induced in vapor pressure prediction as a function of error incurred in *HOV* calculations
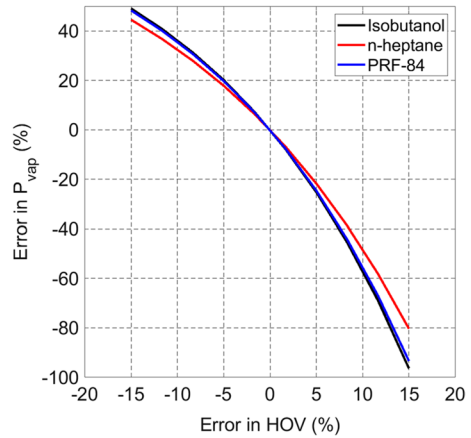
this more advanced scheme, numerical tests are carried out to illustrate the viability of this scheme to predict unknown fuel properties. Figure 11 shows the calculation procedure. The Abramzon–Sirignano (AS) model is used to predict droplet size, velocity, and temperature during the evaporation process with physical properties obtained from reference data sources, in the form of empirical equations as input. Such relationships were obtained for *HOV* [38], vapor pressure [3], and diffusion coefficient [40]. Data from these simulations are then used as inputs along with unknown properties as summarized in Table 1 to perform calculations based on Scheme-II, as described in Appendix B. The Scheme employs a solution of Clausius–Clapeyron and Antoine's equations based on evaporation simulation results, to predict unknown physical properties.

Scheme-II uses droplet temperature measurement, which is otherwise obtained from the steady-state energy balance equation (Eq. 12). This obviates the need to know the vapor specific heat as an input quantity. Further, having the droplet temperature measurement allows for use of the Antoine equation (after estimation of Antoine constants by data-fitting) to find the boiling point of the fuel. Using the Antoine equation, a differential form of the Clausius–Clapeyron equation can be employed to solve for *HOV*, which can reduce the prediction error as compared to Scheme-I. This also allows for accurate prediction of both the LJ parameters (σ and ϵ/k). Results for fuel physical properties obtained from Scheme-II are compared with reference data. Results from the evaporation model, used as inputs for Scheme-II as illustrated in Fig. 11, inherently incorporate model assumptions (Sect. 2), which can be violated by non-ideal conditions in the actual experiment. Thus the fuel property predictions reported through Scheme-II represent a best-case scenario. Exact validation of the Scheme will require measurements at the specific test conditions incorporating droplet velocity and temperature measurements.

Calculations are carried out for evaporation of *n*-heptane droplets at atmospheric pressure while varying the ambient air temperature. All tests use an initial droplet diameter of 36 μm, with an initial velocity of 0.8 m·s^{-1}. These values are consistent with results that are obtained using tests with the current droplet generator

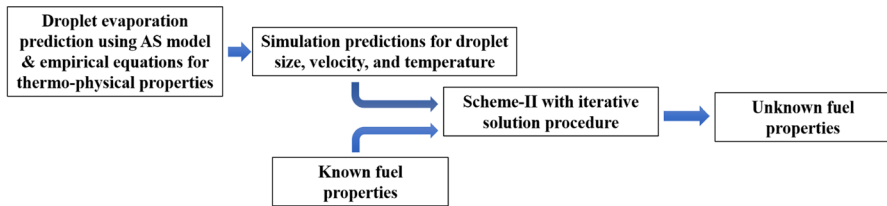**Fig. 11** Fuel property prediction approach using Scheme-II

Table 4 Test conditions for Scheme-II

Case	Fuel	Carrier gas	Inputs			Outputs		
			Initial droplet size	Initial droplet velocity	Carrier gas temperature	Droplet temperature	Evaporation rate	Velocity decay rate
A	*n*-heptane	Air	36	0.8	313.15	292.53	1.59E-8	0.354
B					333.15	300.07	2.51E-8	0.584
C					343.15	303.11	3.06E-8	0.771
D					353.15	305.77	3.60E-8	0.997
E					373.15	310.19	4.71E-8	1.188
F					393.15	313.64	5.85E-8	1.441
			μm	m·s^{-1}	K	K	m^2·s^{-1}	m·s^{-2}

device. Scheme-II expands upon Scheme-I to predict diffusion coefficients and the Lennard–Jones (LJ) potential parameters (σ and ϵ). Diffusion coefficient represents temperature and pressure dependent binary mass diffusion coefficients, which can be used to compute evaporation mass flux along with a concentration gradient. LJ parameters help define the LJ interaction between molecules through the intermolecular potential function [41]. The species-specific LJ parameters are extensively used in determination of transport properties as transport processes are driven by momentum exchange between particles [42, 43]. Table 4 summarizes the test conditions used for Scheme-II, which are categorized as cases from A–F, with varying ambient air temperature. Table 4 also shows outputs from the evaporation model, which are then used with known fuel properties, in Scheme-II, to obtain unknown fuel property predictions, as shown in Fig. 11. Droplet temperature, evaporation rate, and velocity decay rate are all reported at the steady-state condition, defined as when the droplet temperature reaches equilibrium and net heat transfer into the droplet is approximately zero. The increase in velocity decay rate observed in Table 4 is due to an increase in drag coefficient resulting from a decreasing Reynolds number associated with a faster evaporation rate.

Calculations for Scheme-II are pursued with the initial conditions described in Table 4 using the algorithm detailed in Appendix B. Table 5 summarizes the results obtained from the calculations. Table 5 shows temperature-dependent predictions for *HOV*, vapor pressure, diffusion coefficient, and LJ parameters (σ and ϵ/k), along with reference values and prediction error percentage. As can be observed, *HOV*

Table 5 Results from calculations using Scheme-II

Case	HOV [38]			Vapor pressure [3]			Diffusion coefficient [3]			Lennard–Jones parameters [3]		
	Predicted	Reference	Deviation	Predicted	Reference	Deviation	Predicted	Reference	Deviation	Predicted	Reference	Deviation
A	366	367	0.34	4.64	4.60	0.98	7E–6	7.13E–6	2.16	σ		
B	364	363	0.41	6.89	6.89	0.09	7.57E–6	7.63E–6	0.83	6.74	6.25	7.7
C	363	361	0.73	8.08	8.08	0.01	7.82E–6	7.87E–6	0.64	Å		%
D	362.5	359	1.03	9.29	9.28	0.17	8.04E–6	8.11E–6	0.77	ϵ/k		
E	362	356	1.57	11.67	11.63	0.37	8.48E–6	8.55E–6	0.86	425	459.6	8.1
F	360	353	2.03	13.91	13.89	0.12	8.93E–6	8.98E–6	0.56	K		%
	$kJ \cdot kg^{-1}$		%	kPa		%	$m^2 \cdot s^{-1}$		%			

and vapor pressure predictions, using Scheme-II, show considerable improvement as compared to Scheme-I results in Table 3. Deviations in predictions are observed to be 0.3 % to 2 % for *HOV* and 0.01 % to 1 % for vapor pressure. Diffusion coefficients are predicted within 0.6 % to 2 % and deviations in LJ parameter predictions are within 8 % for both σ and ϵ/k. The improvement in Scheme-II predictions primarily arise from the ability to use droplet temperature data as obtained from the simulations to evaluate coefficients in the Antoine's equation and subsequently use the differential form of the Clausius–Clapeyron equation to predict *HOV* resulting in lower deviations from the reference value.

5 Conclusions

The need for small-volume, high-throughput, physical property screening techniques for evaluation of bio-blendstocks with potential to be used as blending components with conventional fuels has motivated the development of droplet evaporation-based property measurement techniques. Evaporation measurements of single droplets at controlled ambient conditions are used in conjunction with transient, zero-dimensional droplet evaporation models and input values for known physical properties to determine unknown properties. This includes temperature-dependent heat of vaporization and vapor pressure. Using the Abramzon–Sirignano droplet evaporation model, two different schemes are proposed, which utilize progressively increasing number of input measurements to generate correspondingly higher number of property predictions. The baseline Scheme-I requires the droplet evaporation rate, while Scheme-II additionally requires droplet velocity and droplet temperature. Scheme-II provides predictions for diffusion coefficients and Lennard–Jones potential parameters, σ and ϵ/k in addition to heat of vaporization and vapor pressure.

A droplet generator-based setup implemented in a temperature-controlled chamber is used with high-resolution imaging to measure droplet evaporation rates for various liquid fuels including *n*-heptane, isobutanol, and PRF 84 which is a blend of 84 % *iso*-octane with 16 % *n*-heptane. Evaporation rates are used with the Scheme-I algorithm to predict temperature-dependent *HOV* and vapor pressure for all three fuels. Deviations of 0.1 % to 9 % and 3 % to 22 % are observed for predictions of *HOV* and vapor pressure, respectively, as compared to reference data from the literature. Deviations for both properties are found to decrease with increasing temperature owing to reduced error in measured droplet evaporation rate given the larger size change, as well as improvements in the prediction algorithm performance. The use of the Clausius–Clapeyron equation is found to make error in vapor pressure predictions highly sensitive to error in *HOV* calculations. Temperature-dependent *HOV* and vapor pressure predictions are interpolated to find *HOV* at 25 °C and the true vapor pressure at 37.8 °C. Predictions show an overall deviation of 2 % to 3 % for *HOV* and 10 % to 15 % for TVP.

Lacking droplet temperature and velocity measurements, Scheme-II is evaluated numerically by using input values generated by droplet evaporation models to carry out the algorithms and make physical property predictions. The availability of droplet velocity and temperature for Scheme-II, along with elimination of experimental droplet

evaporation rate errors, and use of the Clausius–Clapeyron equation in a differential form is found to have a strong influence on error in property predictions. Deviations in property predictions are reduced, with Scheme-II calculations predicting *HOV* and vapor pressure with deviations of 0.3 % to 2 % and 0.01 % to 1 %, respectively. Further, diffusion coefficients and LJ parameters are predicted within 5 % and 8 %, respectively.

Overall, the proposed algorithms in conjunction with experimental measurements show the viability of using droplet evaporation-based techniques for small-volume $\mathcal{O}$ (μl), high-throughput $\mathcal{O}$(ms) screening tools for down selection of liquid fuels on the basis of physical properties relevant to in-cylinder engine processes. Performance of current schemes can be considerably improved by reducing droplet evaporation rate errors through the use of larger droplets as well as higher-resolution imaging techniques. The approach described by Scheme-II has the potential to reduce the number of inputs required for property prediction as well as increase the number and accuracy of predictions. Scheme-II which has been numerically validated in the present work will be evaluated using experimental techniques in future work by incorporating diagnostics for droplet velocity and temperature measurements. Finally, validity of the proposed schemes, which has been limited to alkanes and alcohols in the present work, needs to be examined for more complex fuel mixtures, including additional compounds such as ethers and aromatics.

Appendix A: Property Definition

$$Sh^* = 2 + \frac{(Sh_0 - 2)}{F_M}; \quad Nu^* = 2 + \frac{(Nu_0 - 2)}{F_T}, \tag{A1}$$

$$Sh_0 = 1 + (1 + ReSc)^{1/3}\Phi(Re); \quad Nu_0 = 1 + (1 + RePr)^{1/3}\Phi(Re), \tag{A2}$$

$$F_{(T,M)} = (1 + B_{(T,M)})^{0.7}\frac{\ln(1 + B_{(T,M)})}{B_{(T,M)}}, \tag{A3}$$

where $\Phi(Re) = 1$ for $Re \leq 1$ and $\Phi(Re) = Re^{0.077}$ when $1 < Re \leq 400$

The fuel vapor mass fraction of the film and its temperature are evaluated based on '1/3 rule' recommended in the work of Yuen and Chen [44] given by,

$$\bar{T}_f = T_i + \frac{(T_\infty - T_i)}{3}; \quad \bar{Y}_F = Y_i + \frac{(Y_\infty - Y_i)}{3}. \tag{A4}$$

For the simulations, which provide input to Scheme-II, the empirical diffusion coefficient Eqn.A5 defined in the work of Fuller et. al [40] was employed.

$$\bar{\chi}_{fc} = \frac{0.00143\bar{T}_f^{1.75} \times 10^{-4}}{P_\infty M_{fc}^{0.5}\left(\zeta_c^{1/3} + \zeta_F^{1/3}\right)^2}, \tag{A5}$$

where ζ is the diffusion volume, evaluated based on sum of element wise contributions. For the present study, the diffusion volume for air $\zeta_c = 19.7$ and diffusion volume of n-heptane vapor, $\zeta_F = 148.2$.

Similarly, the temperature-dependent *HOV* of n-heptane is defined based on the handbook of Yaws [38], given by

$$H_F = (A_v(1 - T_i/T_c)^{n_v}) \times 10^6/MW_F; \tag{A6}$$

where for n-heptane, $A_v = 49.73, T_c = 540.26, \& n_v = 0.360$. The temperature-dependent vapor pressure is evaluated by Antoine equation given by,

$$\log_{10}\left(P_{vap}\right) = A - \frac{B}{(C + T_i - 273)}, \tag{A7}$$

where for n-heptane, $A = 4.0404, B = 1263.909, C = 216.432$.

The vapor phase thermal conductivity was defined based on the work of Chung et. al [3], expressed as,

$$k_F = \frac{\mu_F 3.75 \psi R_u}{MW_F}, \tag{A8}$$

$$\psi = 1 + \alpha \left[\frac{(0.215 + 0.28288\alpha - 1.061\beta + 0.2665Z)}{(0.6366 + \beta Z + 1.061\alpha\beta)}\right], \tag{A9}$$

where $\alpha = \dfrac{C_v}{R} - 1.5,\ \beta = 0.7862 - 0.7109\omega + 1.3618\omega^2$ and $Z = 2.0 + 10.5\dfrac{T_f}{T_c}$. T_c represents the critical temperature of the fuel and ω refers to the accentric factor of the fuel. For fuel vapor specific heat and viscosity, fourth order and third order polynomials of temperature are, respectively, employed, with the material specific polynomial coefficients listed in the work of Poling et. al [3] and Yaws et. al [38]

Appendix B: Algorithm for Scheme-II

The pertinent steps of the Scheme-II algorithm are listed below:

1. Using the droplet temperature, experimental data and property inputs as listed in Table. 1, the governing equation for droplet velocity is utilized to solve for interface fuel vapor mass fraction Y_{Fi}. Accordingly, Eq. 2 is interpreted as an implicit function of Y_{Fi} and T_i, as shown below:

$$\frac{du}{dt} + \frac{3C_D\bar{\rho}_f}{4D\rho_l}(u - u_\infty)^2 - g_0\left(1 - \frac{\bar{\rho}_f}{\rho_l}\right) = E(Y_{Fi}, T_i) = 0. \tag{B1}$$

The above equation can be solved for unknown interface mass fraction Y_{Fi}, using any standard root finding technique.

2. The interface mass fraction (Y_{Fi}) is utilized to find the instantaneous vapor pressure of the droplet, which is defined as

$$P_{vap} = P_\infty \left\{ \frac{Y_{Fi} MW_c}{MW_F + Y_{Fi}(MW_c - MW_F)} \right\},$$ (B2)

where MW is the molecular weight of carrier gas (subscript 'c') and fuel (subscript 'F').

3. Using the interface mass fraction and temperature, the mass balance equation Eq. 5 is solved for the unknown film diffusion coefficient $\bar{\chi}_{fc}$, which is expressed as:

$$\bar{\chi}_{fc} = \frac{\dot{m}_l}{\pi \bar{\rho}_f D Sh^* ln(1 + B_M)}.$$ (B3)

4. The above steps are repeated for experiments with different carrier gas temperature. The resulting equilibrium droplet temperature for each experiment and vapor pressure, evaluated from the Step.1 , are employed to find the Antoine constants (A, B, & C) for the tested liquid, by fitting Antoine equation to the experimental data, expressed as,

$$\log_{10} \left(P_{vap} \right) = A - \frac{B}{(C + T_i - 273)}.$$ (B4)

5. Using the Antoine constants in Antoine equation Eq. B4, the boiling point (T_{boil}) of the tested liquid can be determined. Also, *HOV* can be determined by using the differential form of Clausius–Clapeyron equation, given by Eqn. B5, instead of Eqn. 10, which can improve the accuracy of *HOV* predictions.

$$\frac{dP_{vap}}{dT} = \frac{P_{vap} H_F MW_F}{T^2 R_u}.$$ (B5)

6. The predicted diffusion coefficients, for each experiment, is used to evaluate the Lennard–Jones parameters, using the following empirical definition for diffusion coefficient, based on the work of Wilke and Lee [45].

$$\bar{\chi}_{fc} = \frac{[3.03 - (0.98/MW_{fc}^{0.5})](10^{-7})\bar{T}_f^{3/2}}{P_\infty (MW_{fc}^{0.5})\sigma_{fc}^2 \Omega_D},$$ (B6)

where

$$MW_{fc} = 2 \left[\frac{1}{MW_F} + \frac{1}{MW_c} \right]^{-1}$$

$$\sigma_{fc} = \frac{(\sigma_c + \sigma_F)}{2}.$$

The subscript 'c' represents the carrier gas and 'F' represents the fuel vapor. Ω_d represents the collision integral, in terms of Lennard–Jones parameters (σ, ϵ), given by:

$$\Omega_d = \frac{A}{(T^*)^B} + \frac{C}{\exp(DT^*)} + \frac{E}{\exp(FT^*)} + \frac{G}{\exp(HT^*)}, \tag{B7}$$

where

$$T^* = k_b T / \epsilon_{fc} \quad A = 1.06036 \quad B = 0.15610$$
$$C = 0.19300 \quad D = 0.47635 \quad E = 1.03587$$
$$F = 1.52996 \quad G = 1.76474 \quad H = 3.89411$$
$$\epsilon_{fc} = \left(\epsilon_c \epsilon_F\right)^{0.5}$$

The two Lennard–Jones potential (σ, ϵ) parameters are evaluated by non-linear fitting of Eq. B6 on the diffusion coefficient predictions obtained from Step. 6 of the current algorithm. Using the Boiling point T_{boil} evaluated in Step. 1 of the present algorithm, based on the work of Wilke and Lee [45], the Lennard–Jones energy parameter can be defined as $\frac{\epsilon}{k_b} = 1.15 \, T_{boil}$. Using this definition for $\frac{\epsilon}{k_b}$, the diffusion coefficient equation Eq. B6 can be used only to evaluate the Lennard–Jones length (σ), which is observed to improve the prediction accuracy.

References

1. W. Zeng, M. Xu, M. Zhang, Y. Zhang, D.J. Cleary, Macroscopic characteristics for direct-injection multi-hole sprays using dimensionless analysis. Exp. Therm. Fluid Sci. **40**, 81–92 (2012)
2. M.A. Ratcliff, B. Windom, G.M. Fioroni, P.S. John, S. Burke, J. Burton, E.D. Christensen, P. Sindler, R.L. McCormick, Impact of ethanol blending into gasoline on aromatic compound evaporation and particle emissions from a gasoline direct injection engine. Appl. Energy **250**, 1618–1631 (2019)
3. R.C. Reid, J.M. Prausnitz, B.E. Poling, *The Properties of Gases and Liquids* (McGraw Hill Book Co., New York, 1987)
4. L.P. Wyszynski, C.R. Stone, G.T. Kalghatgi, *The Volumetric Efficiency of Direct and Port Injection Gasoline Engines with Different Fuels* (Technical report, SAE Technical Paper, 2002)
5. E.W. Chow, J.B. Heywood, R.L. Speth, (SAE Technical Paper, 2014)
6. M.A. Ratcliff, J.L. Burton, P. Sindler, R.L. McCormick, E.D. Christensen, L.A. Fouts, Effects of heat of vaporization and octane sensitivity on knock-limited spark ignition engine performance. Tech. rep., National Renewable Energy Lab.(NREL), Golden (2018)
7. G.M. Chupka, E. Christensen, L. Fouts, T.L. Alleman, M.A. Ratcliff, R.L. McCormick, Heat of vaporization measurements for ethanol blends up to 50 volume percent in several hydrocarbon blendstocks and implications for knock in si engines. SAE Int. J. Fuels Lubr. **8**, 251–263 (2015)
8. D.A. Splitter, J.P. Szybist, Experimental investigation of spark-ignited combustion with high-octane biofuels and EGR. 2. Fuel and EGR effects on knock-limited load and speed. Energy Fuels **28**, 1432–1445 (2014)
9. G.M. Fioroni, E.D. Christensen, L.A. Fouts, R.L. McCormick, Heat of vaporization and species evolution suring gasoline evaporation measured by dsc/tga/ms for blends of c1 to c4 alcohols in

commercial gasoline blendstocks. Tech. rep., National Renewable Energy Lab.(NREL), Golden (United States) (2019)

10. G. Mendes, H.G. Aleme, P.J. Barbeira, Reid vapor pressure prediction of automotive gasoline using distillation curves and multivariate calibration. Fuel **187**, 167–172 (2017)

11. G.M. Fioroni, L. Fouts, E. Christensen, J.E. Anderson, R.L. McCormick, Measurement of heat of vaporization for research gasolines and ethanol blends by DSC/TGA. Energy Fuels **32**, 12607–12616 (2018)

12. A. Landera, N. Mac Dowell, A. George, Development of robust models for the prediction of Reid vapor pressure (RVP) in fuel blends and their application to oxygenated biofuels using the saft-γ approach. Fuel **283**, 118,624 (2021)

13. I. Hatzioannidis, E.C. Voutsas, E. Lois, D.P. Tassios, Measurement and prediction of Reid vapor pressure of gasoline in the presence of additives. J. Chem. Eng. Data **43**, 386–392 (1998)

14. K. Kar, T. Last, C. Haywood, R. Raine, Measurement of vapor pressures and enthalpies of vaporization of gasoline and ethanol blends and their effects on mixture preparation in an si engine. SAE Int. J. Fuels Lubr. **1**, 132–144 (2009)

15. D.J. Gaspar, S.D. Phillips, E. Polikarpov, K.O. Albrecht, S.B. Jones, A. George, A. Landera, D.M. Santosa, D.T. Howe, A.G. Baldwin et al., Measuring and predicting the vapor pressure of gasoline containing oxygenates. Fuel **243**, 630–644 (2019)

16. R.L. McCormick, G. Fioroni, L. Fouts, E. Christensen, J. Yanowitz, E. Polikarpov, K. Albrecht, D.J. Gaspar, J. Gladden, A. George, Selection criteria and screening of potential biomass-derived streams as fuel blendstocks for advanced spark-ignition engines. SAE Int. J. Fuels Lubr. **10**, 442–460 (2017)

17. W. Dang, W. Zhao, I. Schoegl, S. Menon, A small-volume, high-throughput approach for surface tension and viscosity measurements of liquid fuels. Meas. Sci. Technol. **31**(9) (2020)

18. W. Dang, M. Gurunadhan, I. Schoegl, S. Menon, Temperature effects on droplet oscillation decay with application to fuel property measurement. At. Sprays **31**(10) (2021)

19. H.E. McClelland, P.C. Jurs, Quantitative structure–property relationships for the prediction of vapor pressures of organic compounds from molecular structures. J. Chem. Inf. Comput. Sci. **40**, 967–975 (2000)

20. D.N. Bolmatenkov, M.I. Yagofarov, A.A. Notfullin, B.N. Solomonov, Calculation of the vaporization enthalpies of alkylaromatic hydrocarbons as a function of temperature from their molecular structure. Fluid Phase Equilib. p. 113303 (2021)

21. R. Naef, W.E. Acree Jr., Calculation of the vapour pressure of organic molecules by means of a group-additivity method and their resultant Gibbs free energy and entropy of vaporization at 298.15 k. Molecules **26**, 1045 (2021)

22. S.T. Lin, J. Chang, S. Wang, W.A. Goddard, S.I. Sandler, Prediction of vapor pressures and enthalpies of vaporization using a COSMO solvation model. J. Phys. Chem. A **108**, 7429–7439 (2004)

23. S. Verevkin, V. Emel'yanenko, V. Diky, C. Muzny, R. Chirico, M. Frenkel, New group-contribution approach to thermochemical properties of organic compounds: hydrocarbons and oxygen-containing compounds. J. Phys. Chem. Ref. Data **42**, 033,102 (2013)

24. S.N.R. Isfahani, V.M. Sauer, I. Schoegl, Effects of dilution and pressure on combustion characteristics within externally heated micro-tubes. Proc. Combust. Inst. **38**, 6695–6702 (2021)

25. B. Abramzon, W. Sirignano, Droplet vaporization model for spray combustion calculations. Int. J. Heat Mass Transf. **32**, 1605–1618 (1989)

26. S. Aggarwal, F. Peng, A review of droplet dynamics and vaporization modeling for engineering calculations. J. Eng. Gas Turbines Power **117**, 453–461 (1995)

27. S.S. Sazhin, Advanced models of fuel droplet heating and evaporation. Prog. Energy Combust. Sci. **32**, 162–214 (2006)

28. A.K. Ray, E.J. Davis, P. Ravindran, Determination of ultra-low vapor pressures by submicron droplet evaporation. J. Chem. Phys. **71**, 582–587 (1979)

29. A. Putnam, Integratable form of droplet drag coefficient. ARSJ-Am Rocket Soc. J. **31**, 1467–1468 (1961)

30. F. Foucher, P. Higelin, C. Mounaim-Rousselle, P. Dagaut, Influence of ozone on the combustion of n-heptane in a HCCI engine. Proc. Combust. Inst. **34**, 3005–3012 (2013)

31. Y. Qian, X. Wang, L. Zhu, X. Lu, Experimental studies on combustion and emissions of RCCI (reactivity controlled compression ignition) with gasoline/n-heptane and ethanol/n-heptane as fuels. Energy **88**, 584–594 (2015)

32. S.M. Sarathy, G. Kukkadapu, M. Mehl, W. Wang, T. Javed, S. Park, M.A. Oehlschlaeger, A. Farooq, W.J. Pitz, C.J. Sung, Ignition of alkane-rich face gasoline fuels and their surrogate mixtures. Proc. Combust. Inst. **35**, 249–257 (2015)

33. D.J. Gaspar, B.H. West, D. Ruddy, T.J. Wilke, E. Polikarpov, T.L. Alleman, A. George, E. Monroe, R.W. Davis, D. Vardon, et al., Top ten blendstocks derived from biomass for turbocharged spark ignition engines: bio-blendstocks with potential for highest engine efficiency. Tech. rep., Pacific Northwest National Lab. (PNNL), Richland (2019)

34. S.K. Bhatia, S.H. Kim, J.J. Yoon, Y.H. Yang, Current status and strategies for second generation biofuel production using microbial systems. Energy Convers. Manag. **148**, 1142–1156 (2017)

35. M. Stewart, K. Arnold, *Emulsions and Oil Treating Equipment* (2009), pp. 81–106

36. M. Riazi, T. Albahri, A. Alqattan, Prediction of Reid vapor pressure of petroleum fuels. Pet. Sci. Technol. **23**, 75–86 (2005)

37. A. Baghban, M. Bahadori, Z. Ahmad, T. Kashiwao, A. Bahadori, Modeling of true vapor pressure of petroleum products using Anfis algorithm. Pet. Sci. Technol. **34**, 933–939 (2016)

38. C.L. Yaws, *Thermophysical Properties of Chemicals and Hydrocarbons* (William Andrew, Norwich, 2008)

39. M. Obergruber, V. Honig, P. Prochazka, V. Kucerova, M. Kotek, J. Boucek, J. Marik, Physicochemical properties of biobutanol as an advanced biofuel. Materials **14**, 914 (2021)

40. E.N. Fuller, P.D. Schettler, J.C. Giddings, New method for prediction of binary gas-phase diffusion coefficients. Ind. Eng. Chem. Res. **58**, 18–27 (1966)

41. R.J. Kee, M.E. Coltrin, P. Glarborg, *Chemically Reacting Flow: Theory and Practice* (Wiley, Chichester, 2005)

42. C. Zheng, D.M. Coombs, B. Akih-Kumgeh, Real gas model parameters for high-density combustion from chemical kinetic model data. ACS Omega **4**, 3074–3082 (2019)

43. R.J. Kee, G. Dixon-Lewis, J. Warnatz, M.E. Coltrin, J.A. Miller, A fortran computer code package for the evaluation of gas-phase multicomponent transport properties. Sandia National Laboratories Report SAND86-8246 **13**, 80401 (1986)

44. M. Yuen, L. Chen, On drag of evaporating liquid droplets. Combust. Sci. Technol. **14**, 147–154 (1976)

45. C. Wilke, C. Lee, Estimation of diffusion coefficients for gases and vapors. Ind. Eng. Chem. Res. **47**, 1253–1257 (1955)

Authors and Affiliations

Wanjun Dang[1] [ORCID] · **Mohana Gurunadhan[1]** · **William Ard[1]** · **Ingmar Schoegl[1]** · **Shyam Menon[1]**

✉ Wanjun Dang
   wdang3@lsu.edu

   Mohana Gurunadhan
   mgurun1@lsu.edu

   William Ard
   ward2@lsu.edu

   Ingmar Schoegl
   ischoegl@lsu.edu

   Shyam Menon
   smenon@lsu.edu

[1]   Mechanical and Industrial Engineering Department, Louisiana State University, 3261, Patrick F Taylor Hall, Baton Rouge, LA 70803, USA